

Article

Effect of Cyclic Fatigue Loading on Matrix Multiple Fracture of Fiber-Reinforced Ceramic-Matrix Composites

Longbiao Li 

College of Civil Aviation, Nanjing University of Aeronautics and Astronautics, No.29 Yudao St., Nanjing 210016, China; llb451@nuaa.edu.cn

Received: 24 January 2019; Accepted: 10 May 2019; Published: 13 May 2019



Abstract: In this paper, the effect of cyclic fatigue loading on matrix multiple fracture of fiber-reinforced ceramic-matrix composites (CMCs) is investigated using the critical matrix strain energy (CMSE) criterion. The relationships between multiple matrix cracking, cyclic fatigue peak stress, fiber/matrix interface wear, and debonding are established. The effects of fiber volume fraction, fiber/matrix interface shear stress, and applied cycle number on matrix multiple fracture and fiber/matrix interface debonding and interface wear are discussed. Comparisons of multiple matrix cracking with/without cyclic fatigue loading are analyzed. The experimental matrix cracking of unidirectional SiC/CAS, SiC/SiC, SiC/Borosilicate, and mini-SiC/SiC composites with/without cyclic fatigue loading are predicted.

Keywords: Ceramic-matrix composites (CMCs); Multiple matrix cracking; Cyclic fatigue; Interface debonding; Interface wear

1. Introduction

Advancements in aerospace technology heavily depend on the development of structural materials that maintain mechanical performance at elevated temperatures. Examples of components that are exposed to extreme temperature environments include engine-related components and thermal protection systems. Metals and metallic super-alloys have been developed to increase the temperature capability, but their melting temperatures are being met and exceeded by current and future operating conditions. Ceramics possess excellent high-temperature characteristics, high strength and hardness, chemical inertness, wear resistance, and low density. However, the absence of energy-dissipating mechanisms in ceramics causes catastrophic failure and it precludes their use as structural components. The incorporation of reinforcements in a ceramic matrix, which form a ceramic matrix composite (CMC), has been found to drastically improve the fracture toughness over that of ceramics [1]. CMCs provide a combination of the outstanding thermal and mechanical properties of ceramics with an increased fracture toughness being afforded by the reinforcement phase [2]. CMCs are mainly used in the hot section components of the aero engine, including intermediate temperature/load components (i.e., tail nozzles, etc.), high temperature/intermediate load components (i.e., combustion chamber, afterburner, turbine outer ring, turbine guide vanes, etc.), and high temperature/load components (i.e., turbine blades, etc.) [3]. However, the development of CMCs is in the relatively early stages, and there exists much work to be done in the identification, testing, and characterization of CMCs under a variety of conditions.

Many researchers performed experimental and theoretical investigations on matrix cracking of fiber-reinforced CMCs. The energy balance approach that was suggested by Aveston, Cooper, and Kelly [4], Aveston and Kelly [5], Budiansky, Hutchinson and Evans [6], Chiang [7], Rajan and Zok [8], and Li [9,10], and the fracture mechanics approach that was proposed by Marshall, Cox, and

Evans [11], McCartney [12], Chiang [13], Cox and Marshall [14], and Deng et al. [15], and the stochastic matrix cracking approach that was developed by Ahn and Curtin [16], Lissart and Lamon [17], and Lamon [18], and the critical matrix strain energy (CMSE) approach that was developed by Solti, Mall, and Robertson [19] and Li [20]. Morscher et al. [21] established the relationships for stress-dependent matrix cracking of two-dimensional (2D) Hi-NicalonTM and SylramicTM-iBN SiC fiber-reinforced chemical vapor infiltrated (CVI) SiC matrix composites, which were related to the stress in the load-bearing CVI SiC matrix. Xia et al. [22] developed a coupled electro-mechanical model to predict the matrix cracking of a 2D SiC/SiC composite. The electrical resistance is capable of monitoring damage due to the change in the flow of current through the material when the matrix cracks form and linearly increases with matrix crack density and the number of fiber breaks. Simon et al. [23] developed the electrical model as a network of resistor cells and established a relationship between the electrical resistance and matrix cracking density and debonding density. Li [24,25] investigated the tensile behavior of fiber-reinforced CMCs with different fiber preforms when considering the matrix multi-cracking, interface debonding, and fibers failure. The matrix cracking evolution, saturation matrix cracking stress and density affect the non-linear behavior of CMCs. Under cyclic fatigue loading, the fiber/matrix interface debonding and sliding occurred between matrix crack spacing, leading to interface wear [26,27]. Li et al. [28] investigated the effect of interface bonding properties on cyclic tensile behavior of unidirectional C/Si₃N₄ and SiC/Si₃N₄ composites. The degradation of the interface properties affects the area and shape of the hysteresis loops. The difference of fiber/matrix interface shear stress existed between the interface wear region and the interface debonding region affects matrix multiple cracking evolution with applied stress. Based on the CMSE criterion [19], the matrix cracking density of fiber-reinforced CMCs remains constant under cyclic fatigue loading. However, after the cyclic fatigue loading, the matrix cracking density will increase at the higher stress level than the fatigue peak stress. Simon et al. [29] investigated the behavior of a SiC/[Si-B-C] composite that was tested under air at 450 °C and static and cyclic fatigue conditions, while using electrical resistivity and acoustic emission measurements in order to monitor the ageing of the material. The progression of oxidation through the material could be successfully monitored through the electrical resistivity; however, the matrix cracking density has not been discussed in detail. However, in the studies mentioned above, the effect of cyclic fatigue loading on matrix cracking density of fiber-reinforced CMCs has not been investigated.

In this paper, the effect of cyclic fatigue loading on matrix multiple fracture of fiber-reinforced CMCs is investigated based on the CMSE criterion. When combining with the fiber/matrix interface wear model and fracture mechanics interface debonding criterion, the shear-lag model is adopted to analyze the fiber and matrix axial stress distribution inside of damaged composite. The relationships between multiple matrix cracking, cyclic fatigue peak stress, fiber/matrix interface wear, and debonding are established. The effects of fiber volume fraction, fiber/matrix interface shear stress, and applied cycle number on matrix multiple fracture and fiber/matrix interface debonding and interface wear are discussed. Comparisons of multiple matrix cracking with/without cyclic fatigue loading are analyzed. The experimental matrix cracking of unidirectional SiC/CAS, SiC/SiC, SiC/Borosilicate, and mini-SiC/SiC composites with/without cyclic fatigue loading are predicted. The proposed model applies at ambient temperatures and it excludes any chemical degradation effect.

2. Theoretical Analysis

In this section, the micro stress field of the damage fiber-reinforced CMCs after matrix cracking and interface debonding are obtained while using the shear-lag model. During matrix cracking, the fiber/matrix interface debonding affects the matrix cracking evolution. The interface debonded length is determined using the fracture mechanics approach that is based on the shear-lag micro stress analysis [30]. The degradation law of the interface shear stress with applied cycles is determined using Evan's model [31]. The matrix strain energy for the conditions of interface partial and complete debonding are obtained, and the relationships

between the matrix cracking space, interface debonded length, matrix strain energy, and critical matrix strain energy are established.

2.1. Stress Analysis

Upon first loading to the fatigue peak stress $\sigma_{\max 1}$, matrix cracking and fiber/matrix interface debonding occur. After experiencing N applied cycles, the fiber/matrix interface shear stress in the interface debonded region degrades from the initial value τ_i to τ_f due to the interface wear. Upon increasing applied stress, matrix cracks propagate along the fiber/matrix interface. A unit cell is extracted from the ceramic composite system to analyze the stress distributions in fibers and the matrix, as shown in Figure 1. The unit cell contains a single fiber that is surrounded by a hollow cylinder of matrix. The fiber radius is r_f and the matrix radius is $R(R = r_f/V_f^{1/2})$. The length of the unit cell is $l_c/2$, which is just the half matrix crack space. The fiber/matrix interface debonded length l_d can be divided into two regions, i.e., the interface debonded region with low interface shear stress τ_f ($x \in [0, \zeta]$) and the interface debonded region with high interface shear stress τ_i ($x \in [\zeta, l_d]$), in which ζ denotes the interface debonded length at fatigue peak stress $\sigma_{\max 1}$. On the matrix crack plane, fibers carry all of the stress of σ/V_f , in which σ denotes the far-field applied stress and V_f denotes the fiber volume content. The BHE shear-lag model [6] is adopted to perform the stress and strain analysis in the fiber/matrix interface debonded region ($x \in [0, l_d]$) and interface bonded region ($x \in [l_d, l_c/2]$).

$$\sigma_f(x) = \begin{cases} \frac{\sigma}{V_f} - \frac{2\tau_f}{r_f}x, x \in (0, \zeta) \\ \frac{\sigma}{V_f} - \frac{2\tau_f}{r_f}\zeta - \frac{2\tau_i}{r_f}(x - \zeta), x \in (\zeta, l_d) \\ \sigma_{fo} + \left[\frac{V_m}{V_f}\sigma_{mo} - 2\frac{\tau_f}{r_f}\zeta - 2\frac{\tau_i}{r_f}(l_d - \zeta) \right] \exp\left(-\rho\frac{x-l_d}{r_f}\right), x \in \left(l_d, \frac{l_c}{2}\right) \end{cases} \quad (1)$$

$$\sigma_m(x) = \begin{cases} 2\frac{V_f}{V_m}\frac{\tau_f}{r_f}x, x \in (0, \zeta) \\ 2\frac{V_f}{V_m}\frac{\tau_f}{r_f}\zeta + 2\frac{V_f}{V_m}\frac{\tau_i}{r_f}(x - \zeta), x \in (\zeta, l_d) \\ \sigma_{mo} - \left[\sigma_{mo} - 2\frac{V_f}{V_m}\frac{\tau_f}{r_f}\zeta - 2\frac{V_f}{V_m}\frac{\tau_i}{r_f}(l_d - \zeta) \right] \exp\left(-\rho\frac{x-l_d}{r_f}\right), x \in \left(l_d, \frac{l_c}{2}\right) \end{cases} \quad (2)$$

$$\tau_i(x) = \begin{cases} \tau_f, x \in (0, \zeta) \\ \tau_i, x \in (\zeta, l_d) \\ \frac{\rho}{2} \left[\frac{V_m}{V_f}\sigma_{mo} - 2\frac{\tau_f}{r_f}\zeta - \frac{2\tau_i}{r_f}(l_d - \zeta) \right] \exp\left(-\rho\frac{x-l_d}{r_f}\right), x \in \left(l_d, \frac{l_c}{2}\right) \end{cases} \quad (3)$$

where V_m denotes the matrix volume fraction; ρ denotes the shear-lag model parameter [6]; and, σ_{fo} and σ_{mo} denote the fiber and matrix axial stress in the interface bonded region, respectively.

$$\sigma_{fo} = \frac{E_f}{E_c}\sigma + E_f(\alpha_c - \alpha_f)\Delta T \quad (4)$$

$$\sigma_{mo} = \frac{E_m}{E_c}\sigma + E_m(\alpha_c - \alpha_m)\Delta T \quad (5)$$

where E_f , E_m , and E_c denote the fiber, matrix, and composite elastic modulus, respectively; α_f , α_m , and α_c denote the fiber, matrix, and composite thermal expansion coefficient, respectively; and, ΔT denotes the temperature difference between fabricated temperature T_0 and testing temperature T_1 ($\Delta T = T_1 - T_0$).

$$E_c = V_fE_f + V_mE_m \quad (6)$$

$$\alpha_c = \frac{V_fE_f\alpha_f + V_mE_m\alpha_m}{E_c} \quad (7)$$

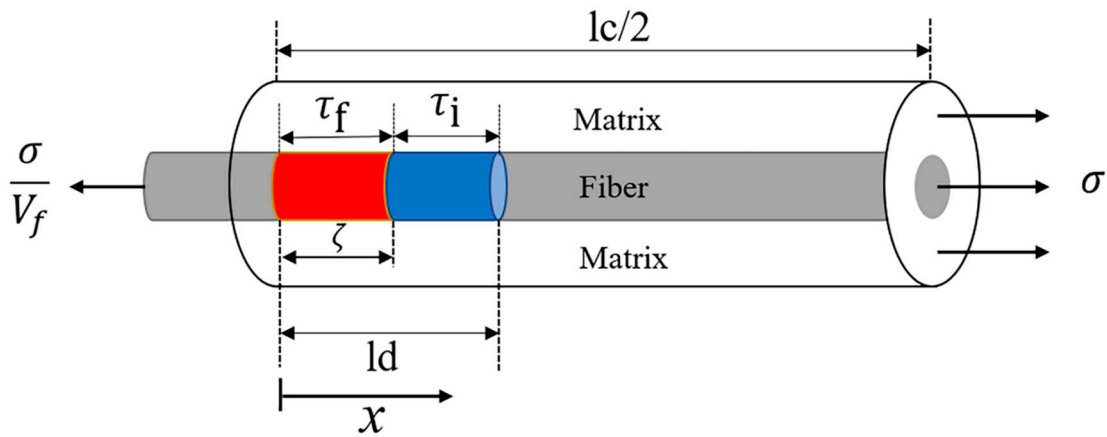


Figure 1. The unit cell of the Budiansky-Hutchinson-Evans shear-lag model.

2.2. Fiber/Matrix Interface Debonding

When matrix cracking propagates to the fiber/matrix interface, it deflects along the interface. The fiber/matrix interface debonded length is determined while using the fracture mechanics approach [30].

$$\xi_d = \frac{F}{4\pi r_f} \frac{\partial w_f(0)}{\partial l_d} - \frac{1}{2} \int_0^{l_d} \tau_i \frac{\partial v(x)}{\partial l_d} dx \tag{8}$$

where $F(= \pi r_f^2 \sigma / V_f)$ denotes the fiber load at the matrix cracking plane; $w_f(0)$ denotes the fiber axial displacement at the matrix cracking plane; and, $v(x)$ denotes the relative displacement between the fibers and matrix. The fiber and matrix axial displacements (i.e., $w_f(x)$ and $w_m(x)$) can be determined using the following equations.

$$\begin{aligned} w_f(x) &= \int_x^{l_c/2} \frac{\sigma_f(x)}{E_f} dx \\ &= \frac{\sigma}{V_f E_f} (l_d - x) - \frac{\tau_f}{r_f E_f} (2\zeta l_d - \zeta^2 - x^2) - \frac{\tau_i}{r_f E_f} (l_d - \zeta)^2 + \frac{\sigma_{fo}}{E_f} \left(\frac{l_c}{2} - l_d\right) \\ &\quad + \frac{r_f}{\rho E_f} \left[\frac{V_m}{V_f} \sigma_{mo} - \frac{2\tau_f}{r_f} \zeta - \frac{2\tau_i}{r_f} (l_d - \zeta) \right] \left[1 - \exp\left(-\rho \frac{l_c/2 - l_d}{r_f}\right) \right] \end{aligned} \tag{9}$$

$$\begin{aligned} w_m(x) &= \int_x^{l_c/2} \frac{\sigma_m(x)}{E_m} dx \\ &= \frac{V_f \tau_f}{r_f V_m E_m} (2\zeta l_d - \zeta^2 - x^2) + \frac{V_f \tau_i}{r_f V_m E_m} (l_d - \zeta)^2 + \frac{\sigma_{mo}}{E_m} \left(\frac{l_c}{2} - l_d\right) \\ &\quad - \frac{r_f}{\rho E_m} \left[\sigma_{mo} - 2 \frac{V_f \tau_f}{r_f V_m} \zeta - 2 \frac{V_f \tau_i}{r_f V_m} (l_d - \zeta) \right] \left[1 - \exp\left(-\rho \frac{l_c/2 - l_d}{r_f}\right) \right] \end{aligned} \tag{10}$$

The relative displacement $v(x)$ between the fiber and the matrix is described using the following equation.

$$\begin{aligned} v(x) &= |w_f(x) - w_m(x)| \\ &= \frac{\sigma}{V_f E_f} (l_d - x) - \frac{E_c \tau_f}{r_f V_m E_m E_f} (2\zeta l_d - \zeta^2 - x^2) - \frac{E_c \tau_i}{r_f V_m E_m E_f} (l_d - \zeta)^2 \\ &\quad + \frac{r_f E_c}{\rho V_m E_m E_f} \left[\sigma_{mo} - 2 \frac{\tau_f}{r_f} \zeta - 2 \frac{\tau_i}{r_f} (l_d - \zeta) \right] \left[1 - \exp\left(-\rho \frac{l_c/2 - l_d}{r_f}\right) \right] \end{aligned} \tag{11}$$

Substituting $w_f(x = 0)$ and $v(x)$ into Equation (8), it leads to the following equation.

$$\begin{aligned} &\frac{E_c \tau_f^2}{r_f V_m E_m E_f} (l_d - \zeta)^2 + \frac{E_c \tau_i^2}{\rho V_m E_m E_f} (l_d - \zeta) - \frac{\tau_i \sigma}{V_f E_f} (l_d - \zeta) + \frac{2E_c \tau_f \tau_i}{r_f V_m E_m E_f} \zeta (l_d - \zeta) \\ &- \frac{r_f \tau_i \sigma}{2\rho V_f E_f} + \frac{E_c \tau_f^2}{r_f V_m E_m E_f} \zeta^2 + \frac{E_c \tau_f \tau_i}{\rho V_m E_m E_f} \zeta - \frac{\tau_f \sigma}{V_f E_f} \zeta + \frac{r_f V_m E_m \sigma^2}{4V_f^2 E_f E_c} - \xi_d = 0 \end{aligned} \tag{12}$$

Solve Equation (12), the fiber/matrix interface debonded length is determined using the following equation.

$$l_d = \left(1 - \frac{\tau_f}{\tau_i}\right)\zeta + \frac{r_f}{2} \left(\frac{V_m E_m \sigma}{V_f E_c \tau_i} - \frac{1}{\rho}\right) - \sqrt{\left(\frac{r_f}{2\rho}\right)^2 + \frac{r_f V_m E_m E_f}{E_c \tau_i^2} \zeta_d} \tag{13}$$

where

$$\zeta = \frac{r_f}{2} \left(\frac{V_m E_m \sigma_{max}}{V_f E_c \tau_i(N)} - \frac{1}{\rho}\right) - \sqrt{\left(\frac{r_f}{2\rho}\right)^2 + \frac{r_f V_m E_m E_f}{E_c \tau_i^2} \zeta_d} \tag{14}$$

where $\tau_i(N)$ denotes the cyclic-dependent interface shear stress.

2.3. Fiber/Matrix Interface Wear

When a CMC is subjected to a cyclic loading between a peak stress and a valley stress, the fiber/matrix interface shear stress degrades with increasing applied cycle numbers due to the interface wear. The degradation of fiber/matrix interface shear stress with increasing applied cycles can be described while using the following equation. [31]

$$\tau_i(N) = \tau_{i0} + [1 - \exp(-\omega N^\lambda)](\tau_{imin} - \tau_{i0}) \tag{15}$$

where τ_{i0} denotes the initial fiber/matrix interface shear stress; τ_{imin} denotes the steady-state fiber/matrix interface shear stress; and, ω and λ are empirical constants. Evans et al. [31] investigated the fatigue behavior of unidirectional SiC/CAS composite at room temperature and obtained the interface shear stress using hysteresis analysis. Under the fatigue peak stress of $\sigma_{max} = 280$ MPa, the interface shear stress degraded from $\tau_{i0} = 22$ MPa to $\tau_{imin} = 5$ MPa during the first 100 cycles. Figure 2 shows the experimental and predicted interface shear stress versus the applied cycles curves, and the empirical constants are given by $\omega = 0.001$ and $\lambda = 3.2$.

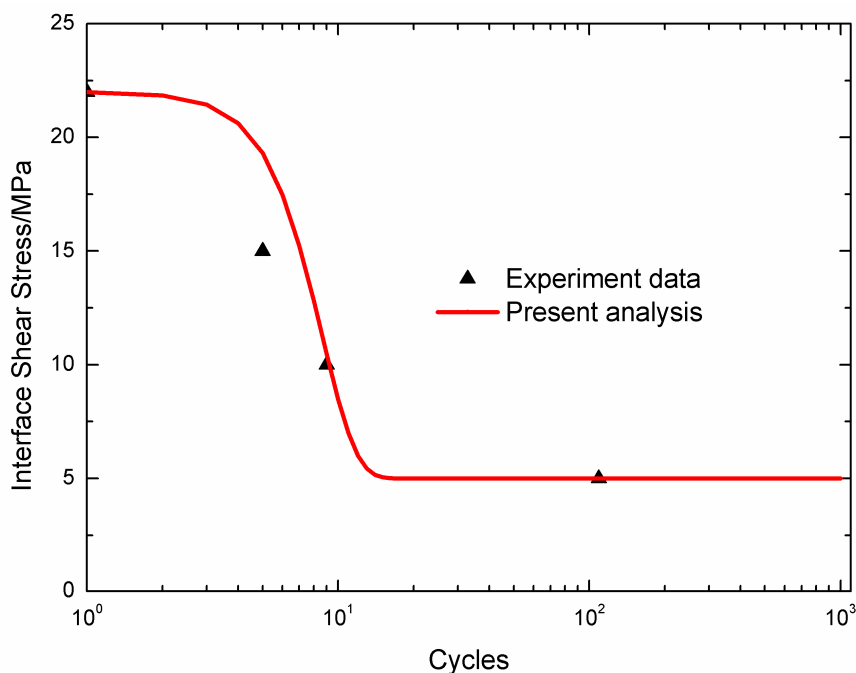


Figure 2. The experimental and predicted interface shear stress versus the applied cycles curves of unidirectional SiC/CAS composite.

2.4. Matrix Multiple Fracture

The matrix strain energy is determined using the following equation.

$$U_m = \frac{1}{2E_m} \int_{A_m} \int_0^{l_c} \sigma_m^2(x) dx dA_m \tag{16}$$

where A_m is the cross-section area of matrix in the unit cell. While substituting the matrix axial stress in Equation (2) into Equation (16), the matrix strain energy considering matrix cracking and fiber/matrix interface partially debonding, is described using the following equation.

$$U_m = \frac{A_m}{E_m} \left\{ \frac{4}{3} \left(\frac{V_f \tau_f}{V_m r_f} \right)^2 \zeta^3 + 4 \left(\frac{V_f \tau_f}{V_m r_f} \right)^2 \zeta^2 (l_d - \zeta) + 4 \left(\frac{V_f}{r_f V_m} \right)^2 \tau_f \tau_i \zeta (l_d - \zeta)^2 + \frac{4}{3} \left(\frac{V_f \tau_i}{V_m r_f} \right)^2 (l_d - \zeta)^3 + \sigma_{mo}^2 \left(\frac{l_c}{2} - l_d \right) + \frac{2r_f \sigma_{mo}}{\rho} \left[2 \frac{V_f \tau_f}{V_m r_f} \zeta + 2 \frac{V_f \tau_i}{V_m r_f} (l_d - \zeta) - \sigma_{mo} \right] \left[1 - \exp\left(-\rho \frac{l_c/2 - l_d}{r_f} \right) \right] + \frac{r_f}{2\rho} \left[2 \frac{V_f \tau_f}{V_m r_f} \zeta + 2 \frac{V_f \tau_i}{V_m r_f} (l_d - \zeta) - \sigma_{mo} \right]^2 \left[1 - \exp\left(-2\rho \frac{l_c/2 - l_d}{r_f} \right) \right] \right\} \tag{17}$$

When the fiber/matrix interface completely debonds, the matrix strain energy is described using the following equation.

$$U_m(\sigma, l_c, l_d = l_c/2) = \frac{A_m}{E_m} \left[\frac{4}{3} \left(\frac{V_f \tau_f}{V_m r_f} \right)^2 \zeta^3 + 4 \left(\frac{V_f \tau_f}{V_m r_f} \right)^2 \zeta^2 (l_d - \zeta) + 4 \left(\frac{V_f}{r_f V_m} \right)^2 \tau_f \tau_i \zeta (l_d - \zeta)^2 + \frac{4}{3} \left(\frac{V_f \tau_i}{V_m r_f} \right)^2 (l_d - \zeta)^3 \right] \tag{18}$$

When evaluating the matrix strain energy at a critical stress of σ_{cr} , the critical matrix strain energy of U_{crm} can be obtained. The critical matrix strain energy is described using the following equation.

$$U_{crm} = \frac{1}{2} k A_m l_0 \frac{\sigma_{mocr}^2}{E_m} \tag{19}$$

where k ($k \in [0,1]$) is the critical matrix strain energy parameter; and, l_0 is the initial matrix crack spacing and σ_{mocr} is determined using the following equation.

$$\sigma_{mocr} = \frac{E_m}{E_c} \sigma_{cr} + E_m (\alpha_c - \alpha_m) \Delta T \tag{20}$$

where σ_{cr} is the critical stress corresponding to composite's proportional limit stress, i.e., the stress at which the stress/strain curve starts to deviate from linearity due to the damage accumulation of matrix cracks [32]. The critical stress is defined to be Aveston-Cooper-Kelly (ACK) matrix cracking stress, and it is determined using the following equation [4].

$$\sigma_{cr} = \left(\frac{6V_f^2 E_f E_c^2 \tau_i \xi_m}{r_f V_m E_m^2} \right)^{\frac{1}{3}} - E_c (\alpha_c - \alpha_m) \Delta T \tag{21}$$

where ξ_m denotes the matrix fracture energy.

The energy balance relationship to evaluate multiple matrix cracking is determined using the following equation.

$$U_m(\sigma > \sigma_{cr}, l_c, l_d) = U_{crm}(\sigma_{cr}, l_0) \tag{22}$$

Equation (22) can solve the multiple matrix cracking versus the applied stress when the critical matrix cracking stress σ_{cr} and the fiber/matrix interface debonded length l_d are determined by Equations (13) and (21).

The matrix cracking density of ψ can be determined using the following equation.

$$\psi = \frac{1.0}{l_c} \quad (23)$$

3. Results and Discussions

The ceramic composite system of unidirectional SiC/CAS is used for the case study and its material properties are given by: $V_f = 30\%$, $E_f = 200$ GPa, $E_m = 97$ GPa, $r_f = 7.5$ μm , $\xi_m = 6$ J/m², $\xi_d = 0.8$ J/m², $\tau_i = 25$ MPa, $\tau_f = 5$ MPa, $\alpha_f = 4 \times 10^{-5}/^\circ\text{C}$, $\alpha_m = 5 \times 10^{-5}/^\circ\text{C}$, $\Delta T = -1000$ $^\circ\text{C}$. The effects of fiber volume fraction, fiber/matrix interface shear stress and applied cycle number on matrix cracking density, fiber/matrix interface debonded length, fiber/matrix interface debonding ratio, and fiber/matrix interface wear ratio are discussed. The comparisons of matrix cracking with and without fatigue loading are also analyzed.

3.1. Effect of Fiber Volume Fraction on Matrix Multiple Fracture and Fiber/Matrix Interface Debonding

Figure 3 shows the matrix cracking density (ψ), fiber/matrix interface debonded length (l_d/r_f), the interface debonding ratio ($2l_d/l_c$), and interface wear ratio (ζ/l_d) corresponding to different fiber volume contents (i.e., $V_f = 30\%$ and 35%).

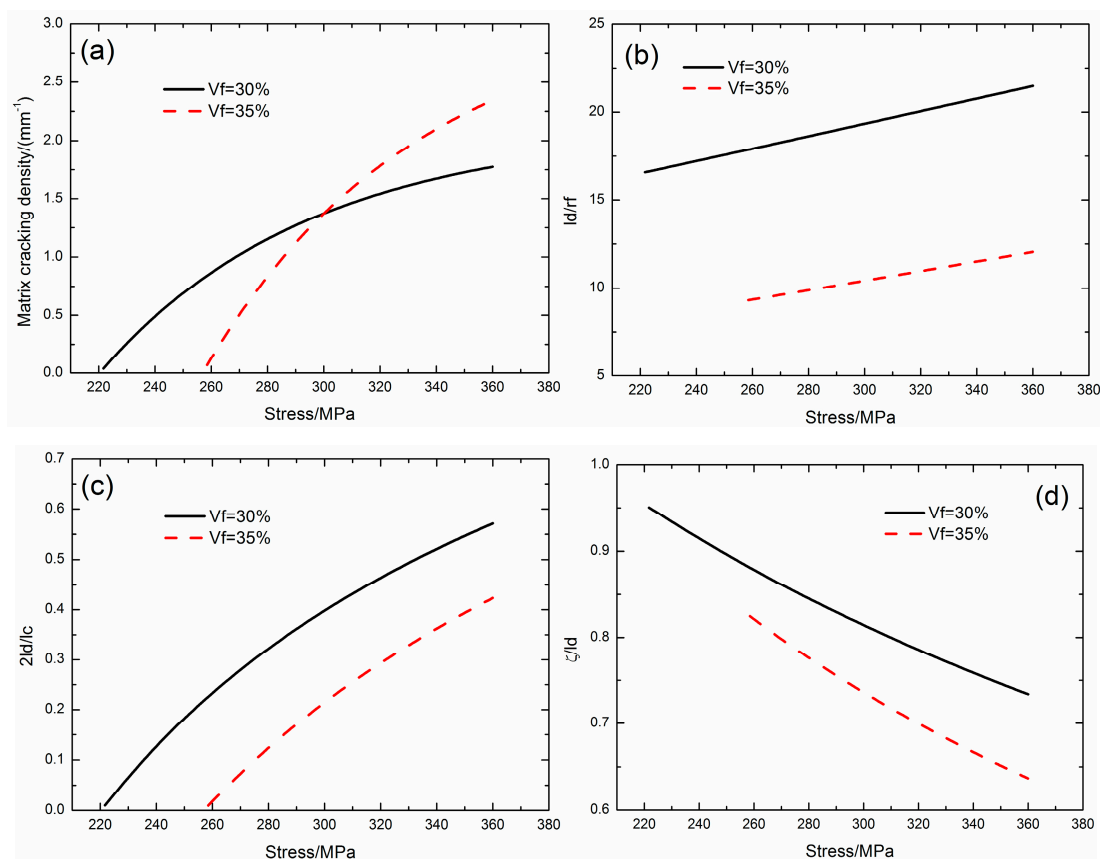


Figure 3. The prediction effect of fiber volume fraction (i.e., $V_f = 30\%$ and 35%) on (a) the matrix cracking density versus applied stress curves; (b) the fiber/matrix interface debonded length (l_d/r_f) versus applied stress curves; (c) the fiber/matrix interface debonding ratio ($2l_d/l_c$) versus applied stress curves; and, (d) the fiber/matrix interface wear ratio (ζ/l_d) versus applied stress curves.

When the fiber volume content is $V_f = 30\%$, the matrix cracking density increases from $\psi = 0.04/\text{mm}$ at the first matrix cracking stress of $\sigma_{mc} = 221$ MPa to $\psi = 1.7/\text{mm}$ at the matrix cracking stress of

360 MPa; the fiber/matrix interface debonded length increases from $l_d/r_f = 16.5$ to $l_d/r_f = 21.5$; the fiber/matrix interface debonding ratio increases from $2l_d/l_c = 0.9\%$ to $2l_d/l_c = 57.1\%$; and, the fiber/matrix interface wear ratio decreases from $\zeta/l_d = 95\%$ to $\zeta/l_d = 73.3\%$.

When the fiber volume content is $V_f = 35\%$, the matrix cracking density increases from $\psi = 0.06/\text{mm}$ at the first matrix cracking stress of $\sigma_{mc} = 258$ MPa to $\psi = 2.3/\text{mm}$ at the matrix cracking stress of 360 MPa; the fiber/matrix interface debonded length increases from $l_d/r_f = 9.3$ to $l_d/r_f = 12$; the fiber/matrix interface debonding ratio increases from $2l_d/l_c = 0.9\%$ to $2l_d/l_c = 42.3\%$; and, the fiber/matrix interface wear ratio decreases from $\zeta/l_d = 82.4\%$ to $\zeta/l_d = 63.6\%$.

With the increasing of the fiber volume fraction, the first matrix cracking stress, matrix saturation cracking stress, and matrix cracking density increase; and, the fiber/matrix interface debonded length, fiber/matrix interface debonding ratio, and interface wear ratio decrease. When the fiber volume fraction increases, the stress transfer between the fiber and matrix increases, which increases the matrix strain energy and decreases the matrix crack spacing approaching to the critical matrix strain energy.

3.2. Effect of Fiber/Matrix Interface Shear Stress on Matrix Multiple Fracture and Fiber/Matrix Interface Debonding

Figure 4 shows the matrix cracking density (ψ), fiber/matrix interface debonded length (l_d/r_f), fiber/matrix interface debonding ratio ($2l_d/l_c$), and fiber/matrix interface wear ratio (ζ/l_d) corresponding to different fiber/matrix interface shear stress (i.e., $\tau_i = 20$ and 30 MPa).

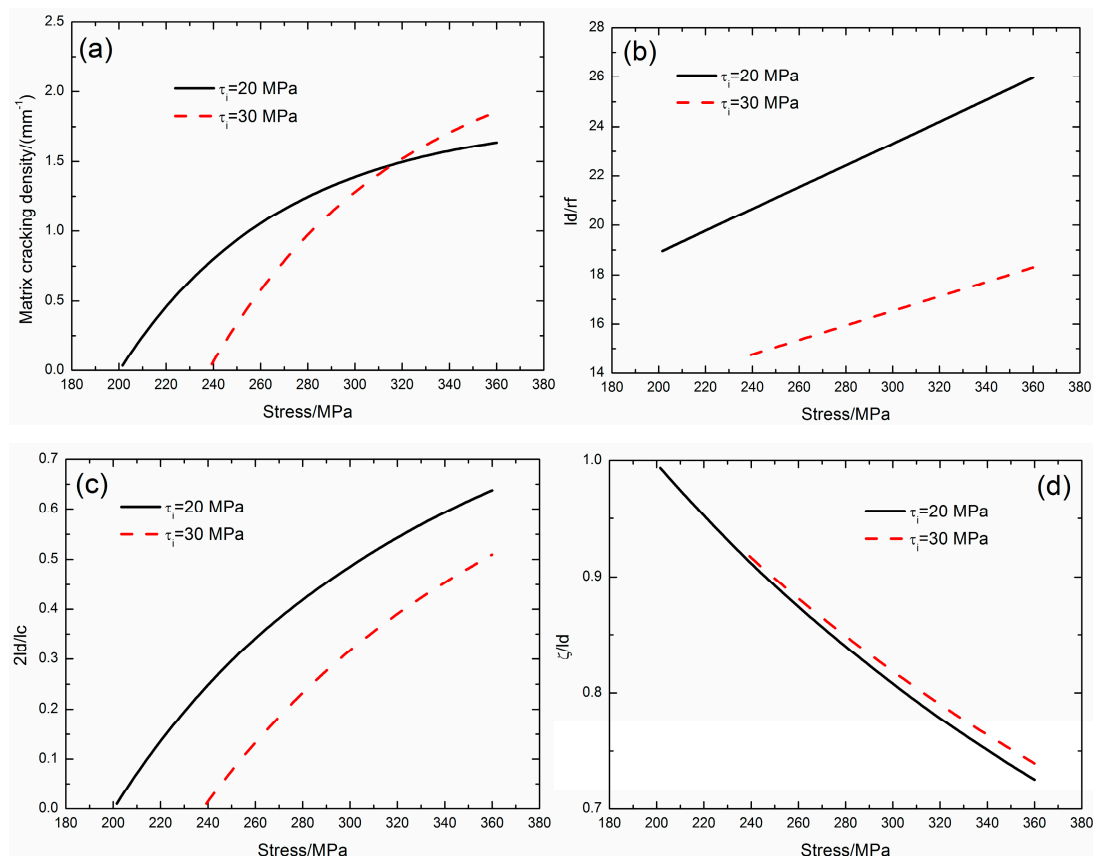


Figure 4. The prediction effect of fiber/matrix interface shear stress (i.e., $\tau_i = 20$ and 30 MPa) on (a) the matrix cracking density versus applied stress curves; (b) the fiber/matrix interface debonded length (l_d/r_f) versus applied stress curves; (c) the fiber/matrix interface debonding ratio ($2l_d/l_c$) versus applied stress curves; and, (d) the fiber/matrix interface wear ratio (ζ/l_d) versus applied stress curves.

When the fiber/matrix interface shear stress is $\tau_i = 20$ MPa, the matrix cracking density increases from $\psi = 0.03/\text{mm}$ at the first matrix cracking stress of $\sigma_{mc} = 201$ MPa to $\psi = 1.6/\text{mm}$ at the matrix cracking stress of 360 MPa; the fiber/matrix interface debonded length increases from $l_d/r_f = 18.9$ to $l_d/r_f = 25.9$; the fiber/matrix interface debonding ratio increases from $2l_d/l_c = 0.9\%$ to $2l_d/l_c = 63.7\%$; and, the fiber/matrix interface wear ratio decreases from $\zeta/l_d = 99.3\%$ to $\zeta/l_d = 72.5\%$.

When the fiber/matrix interface shear stress is $\tau_i = 30$ MPa, the matrix cracking density increases from $\psi = 0.04/\text{mm}$ at the first matrix cracking stress of $\sigma_{mc} = 239$ MPa to $\psi = 1.8/\text{mm}$ at the matrix cracking stress of 360 MPa; the fiber/matrix interface debonded length increases from $l_d/r_f = 14.7$ to $l_d/r_f = 18.2$; the fiber/matrix interface debonding ratio increases from $2l_d/l_c = 0.9\%$ to $2l_d/l_c = 50.9\%$; and, the fiber/matrix interface wear ratio decreases from $\zeta/l_d = 91.7\%$ to $\zeta/l_d = 73.9\%$.

With increasing fiber/matrix interface shear stress, the first matrix cracking stress, saturation matrix cracking stress, and matrix cracking density increase; and, the fiber/matrix interface debonded length and interface debonding ratio decrease; and, the fiber/matrix interface wear ratio increases.

When the interface shear stress increases, the stress transfer between the fiber and matrix increases, which increases the matrix strain energy and decreases the matrix crack spacing approaching to the critical matrix strain energy.

3.3. Effect of Applied Cycle Number on Matrix Multiple Fracture and Interface Debonding

Figure 5 shows the matrix cracking density (ψ), fiber/matrix interface debonded length (l_d/r_f), fiber/matrix interface debonding ratio ($2l_d/l_c$), and fiber/matrix interface wear ratio (ζ/l_d) corresponding to different applied cycles of $N = 100, 1000$, and 2000 at the fatigue peak stress of $\sigma_{\max 1} = 200$ MPa.

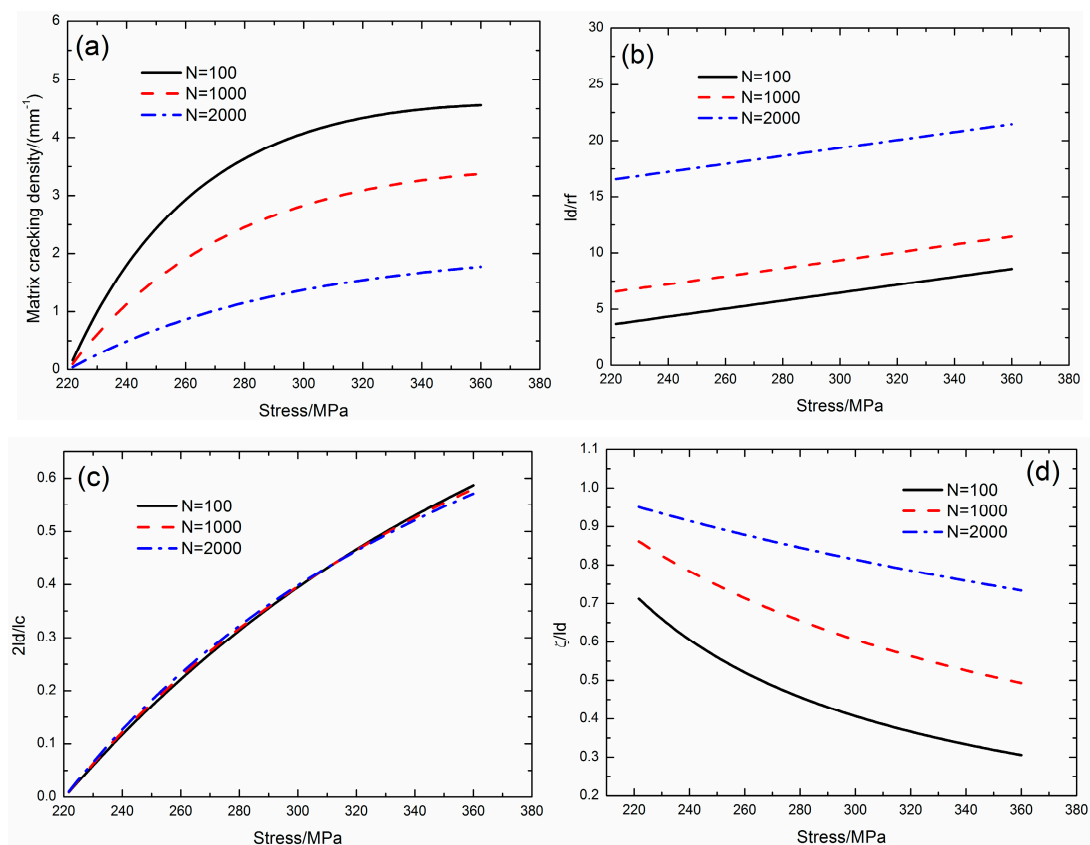


Figure 5. The prediction effect of applied cycle number (i.e., $N = 100, 1000$ and 2000) on (a) the matrix cracking density versus applied stress curves; (b) the fiber/matrix interface debonded length (l_d/r_f) versus applied stress curves; (c) the fiber/matrix interface debonding ratio ($2l_d/l_c$) versus applied stress curves; and, (d) the fiber/matrix interface wear ratio (ζ/l_d) versus applied stress curves.

When the applied cycle number is $N = 100$, the matrix cracking density increases from $\psi = 0.16/\text{mm}$ at the first matrix cracking stress of $\sigma_{\text{mc}} = 221$ MPa to $\psi = 4.5/\text{mm}$ at the saturation matrix cracking stress of $\sigma_{\text{sat}} = 360$ MPa; the fiber/matrix interface debonded length increases from $l_d/r_f = 3.6$ to $l_d/r_f = 8.5$; the fiber/matrix interface debonding ratio increases from $2l_d/l_c = 0.8\%$ to $2l_d/l_c = 58.6\%$; and, the fiber/matrix interface wear ratio decreases from $\zeta/l_d = 71.2\%$ to $\zeta/l_d = 30.6\%$.

When the applied cycle number is $N = 1000$, the matrix cracking density increases from $\psi = 0.09/\text{mm}$ at the first matrix cracking stress of $\sigma_{\text{mc}} = 221$ MPa to $\psi = 3.3/\text{mm}$ at the saturation matrix cracking stress of $\sigma_{\text{sat}} = 360$ MPa; the fiber/matrix interface debonding length increases from $l_d/r_f = 6.5$ to $l_d/r_f = 11.4$; the fiber/matrix interface debonding ratio increases from $2l_d/l_c = 0.9\%$ to $2l_d/l_c = 58\%$; and, the fiber/matrix interface wear ratio decreases from $\zeta/l_d = 86.1\%$ to $\zeta/l_d = 49.3\%$.

When the applied cycle number is $N = 2000$, the matrix cracking density increases from $\psi = 0.04/\text{mm}$ at the first matrix cracking stress of $\sigma_{\text{mc}} = 221$ MPa to $\psi = 1.7/\text{mm}$ at the saturation matrix cracking stress of $\sigma_{\text{sat}} = 360$ MPa; the fiber/matrix interface debonded length increases from $l_d/r_f = 16.5$ to $l_d/r_f = 21.4$; the fiber/matrix interface debonding ratio increases from $2l_d/l_c = 0.9\%$ to $2l_d/l_c = 57.1\%$; and, the fiber/matrix interface wear ratio decreases from $\zeta/l_d = 95\%$ to $\zeta/l_d = 73.3\%$.

With increasing the applied cycle number, the interface shear stress decreases, and the matrix cracking density decreases; and the fiber/matrix interface debonded length and interface wear ratio increase. When the applied cycles increase, the interface shear stress decreases, and the stress transfer between the fiber and the matrix also decreases, which leads to the decrease of the matrix strain energy and the increase of the matrix crack spacing approaching to the critical matrix strain energy.

3.4. Comparisons with/without Fatigue Loading

Comparisons of matrix cracking density (ψ), fiber/matrix interface debonding ratio ($2l_d/l_c$), and fiber/matrix interface wear ratio with/without cyclic fatigue loading (Case 1, $\sigma_{\text{max}1} = 200$ MPa and $N = 1000$; and, Case 2, $\sigma_{\text{max}1} = 200$ MPa and $N = 2000$) are shown in Figure 6.

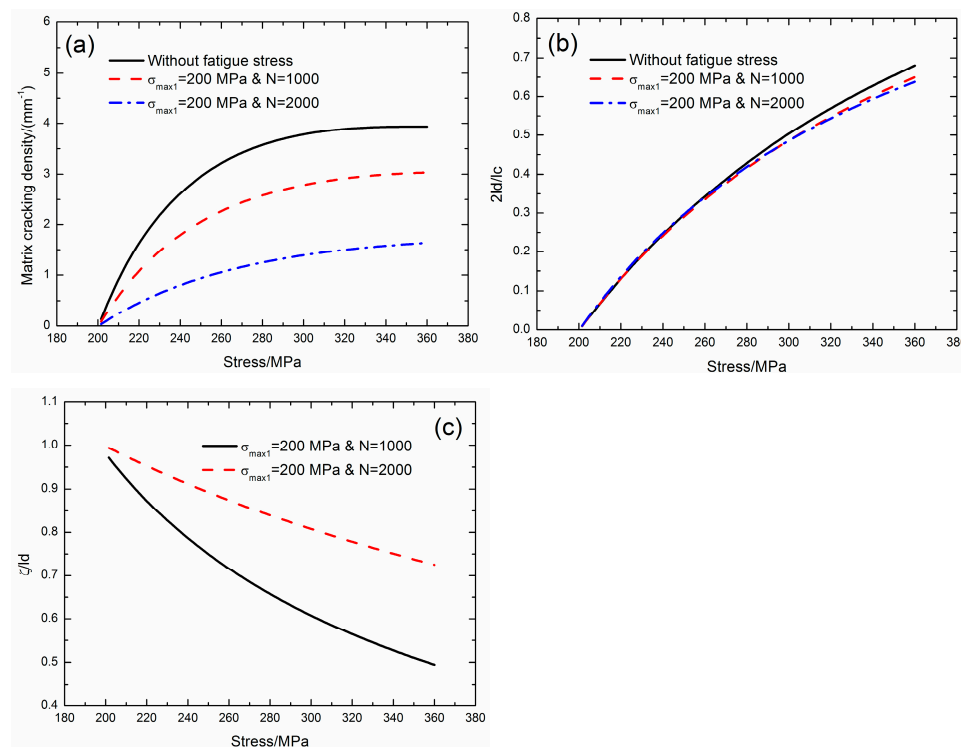


Figure 6. The comparisons of with/without fatigue loading for (a) matrix cracking density versus applied stress curves; (b) the fiber/matrix interface debonding ratio ($2l_d/l_c$) versus applied stress curves; and, (c) the fiber/matrix interface wear ratio (ζ/l_d) versus applied stress curves.

Without considering cyclic fatigue loading, the matrix cracking density increases from $\psi = 0.13/\text{mm}$ at the first matrix cracking stress of $\sigma_{\text{mc}} = 201 \text{ MPa}$ to $\psi = 3.9/\text{mm}$ at the saturation matrix cracking stress of $\sigma_{\text{sat}} = 360 \text{ MPa}$; and, the fiber/matrix interface debonding ratio increases from $2l_d/l_c = 0.92\%$ to $2l_d/l_c = 68\%$.

When considering cyclic fatigue loading for Case 1 (i.e., $\sigma_{\text{max1}} = 200 \text{ MPa}$ and $N = 1000$), the matrix cracking density increases from $\psi = 0.08/\text{mm}$ at the first matrix cracking stress of $\sigma_{\text{mc}} = 201 \text{ MPa}$ to $\psi = 3.0/\text{mm}$ at the saturation matrix cracking stress of $\sigma_{\text{sat}} = 360 \text{ MPa}$; the fiber/matrix interface debonding ratio increases from $2l_d/l_c = 0.94\%$ to $2l_d/l_c = 64.9\%$; and, the fiber/matrix interface wear ratio decreases from $\zeta/l_d = 97.1\%$ to $\zeta/l_d = 49.4\%$. For Case 2 (i.e., $\sigma_{\text{max1}} = 200 \text{ MPa}$ and $N = 2000$), the matrix cracking density increases from $\psi = 0.03/\text{mm}$ at the first matrix cracking stress of 201 MPa to $\psi = 1.6/\text{mm}$ at the saturation matrix cracking stress of $\sigma_{\text{sat}} = 360 \text{ MPa}$; the fiber/matrix interface debonding ratio increases from $2l_d/l_c = 0.99\%$ to $2l_d/l_c = 63.7\%$; and, the fiber/matrix interface wear ratio decreases from $\zeta/l_d = 99.3\%$ to $\zeta/l_d = 72.5\%$.

Under cyclic fatigue loading, the fiber/matrix interface shear stress degrades with applied cycles due to the interface wear. When considering fiber/matrix interface wear, the matrix cracking density and the fiber/matrix interface debonding ratio decrease.

4. Experimental Comparisons

The experimental and theoretical matrix cracking density (ψ), fiber/matrix interface debonded ratio ($2l_d/l_c$), and fiber/matrix interface wear ratio (ζ/l_d) versus the applied stress for different fiber-reinforced CMCs, i.e., unidirectional SiC/CAS-II [33], SiC/SiC [34], SiC/CAS [35], SiC/Borosilicate [36], and mini-SiC/SiC [37] composites are predicted, as shown in Figures 7–11. Table 1 lists the material properties of fiber-reinforced CMCs. The parameters of ω and λ listed in Table 1 are identified using the present approach.

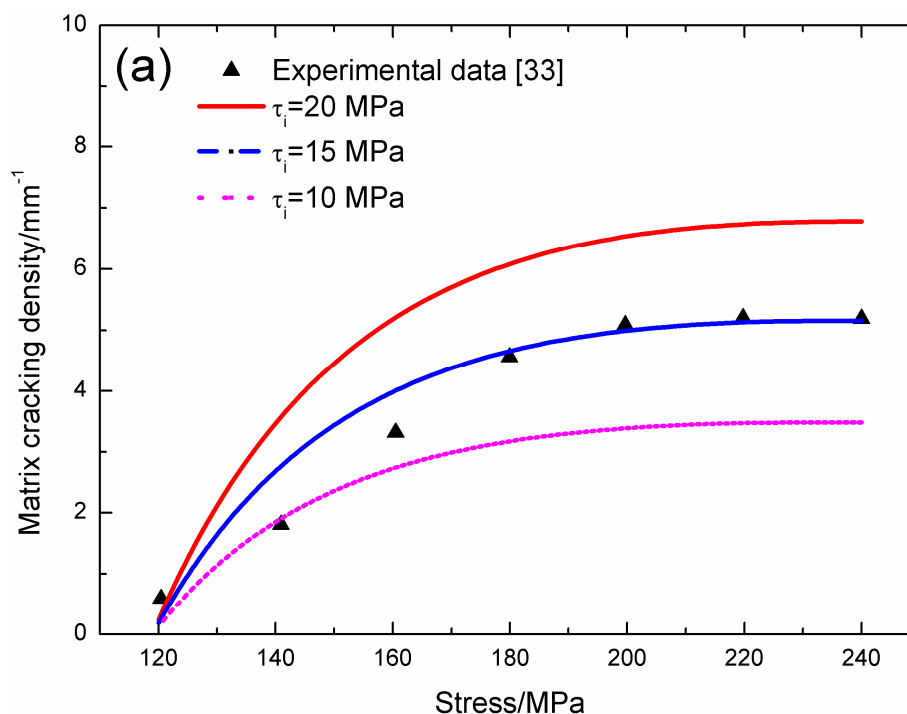


Figure 7. Cont.

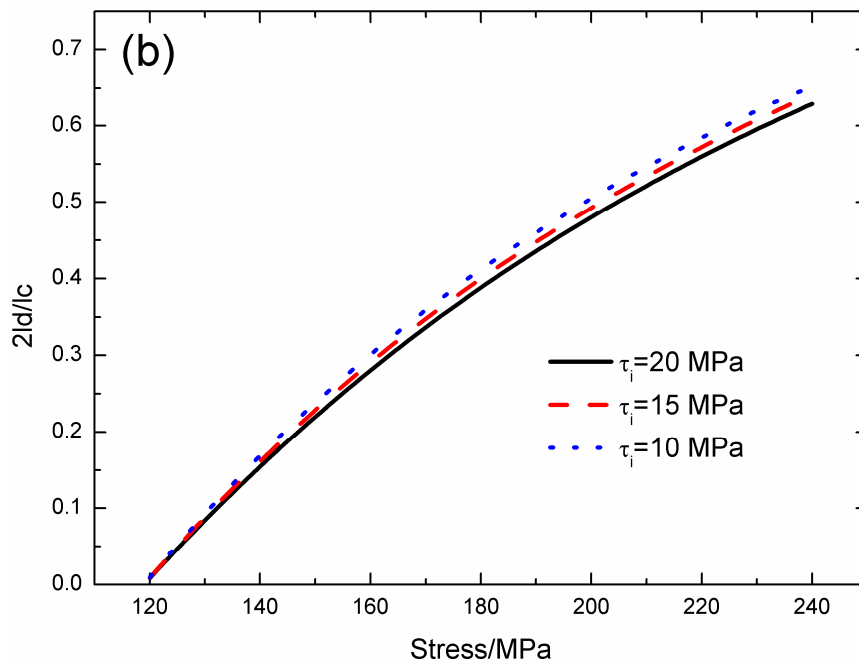


Figure 7. (a) The experimental and predicted matrix cracking density versus the applied stress curves; and (b) the fiber/matrix interface debonded length versus the applied stress curves of the unidirectional SiC/CAS-II composite [33].

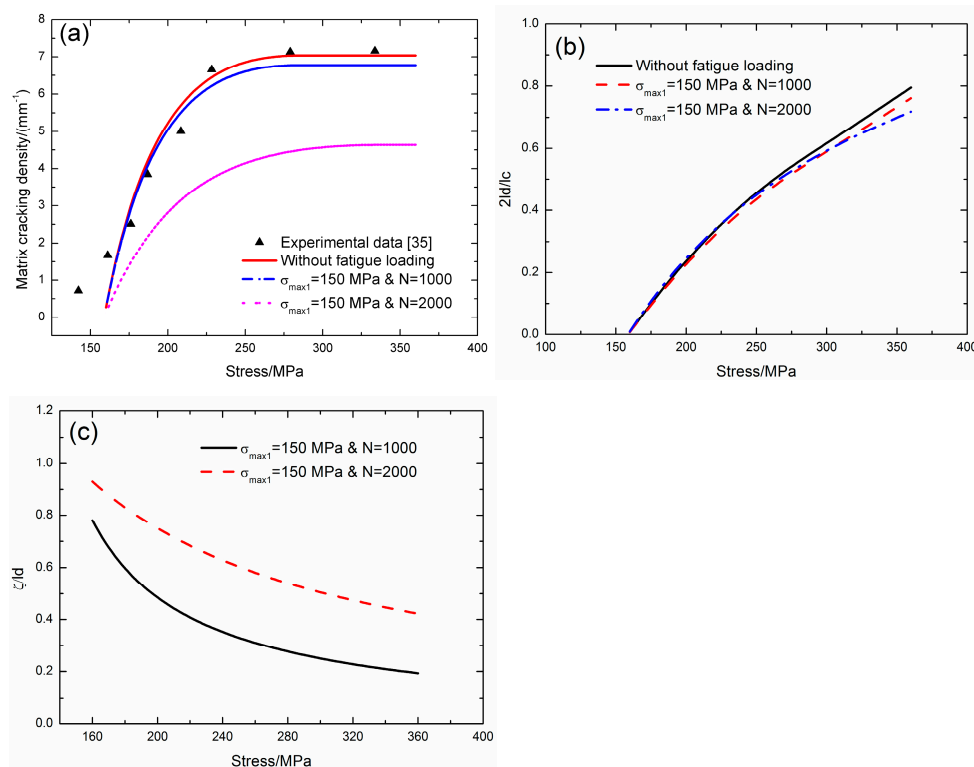


Figure 8. (a) The experimental and theoretical matrix cracking density versus applied stress curves; (b) the fiber/matrix interface debonded ratio ($2l_d/l_c$) versus applied stress curves; and (c) the fiber/matrix interface wear ratio (ζ/l_d) of unidirectional SiC/CAS composite with/without fatigue loading [35].

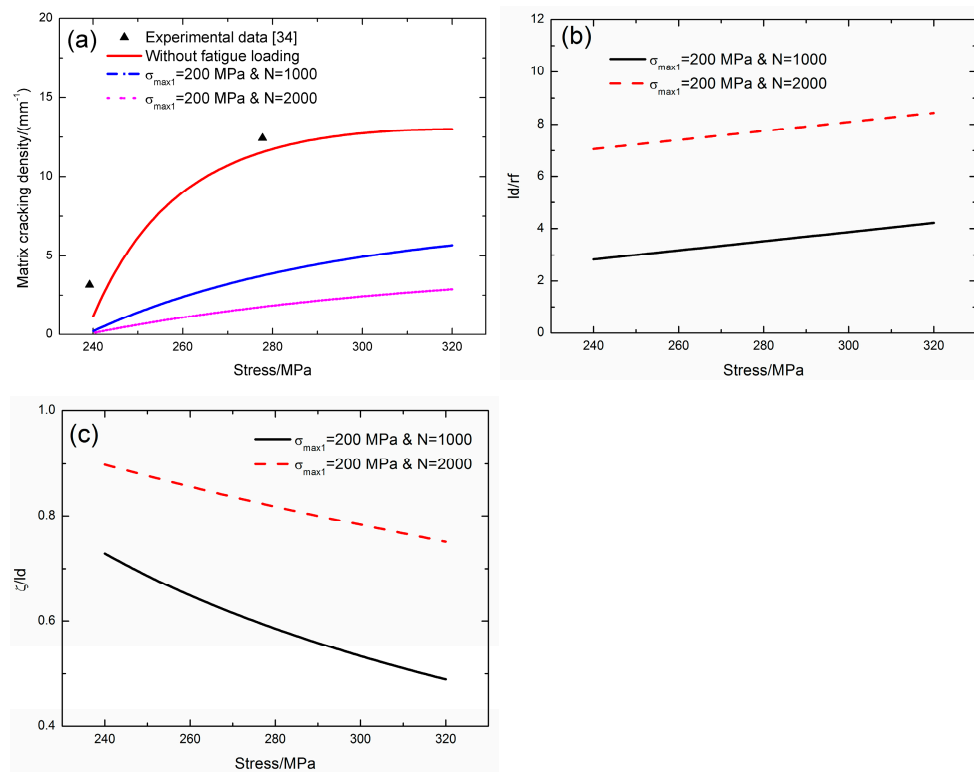


Figure 9. (a) The experimental and theoretical matrix cracking density versus applied stress curves; (b) the fiber/matrix interface debonded length (l_d/r_f) versus applied stress curves; and, (c) the fiber/matrix interface wear ratio (ζ/l_d) of unidirectional SiC/SiC composite with/without fatigue loading [34].

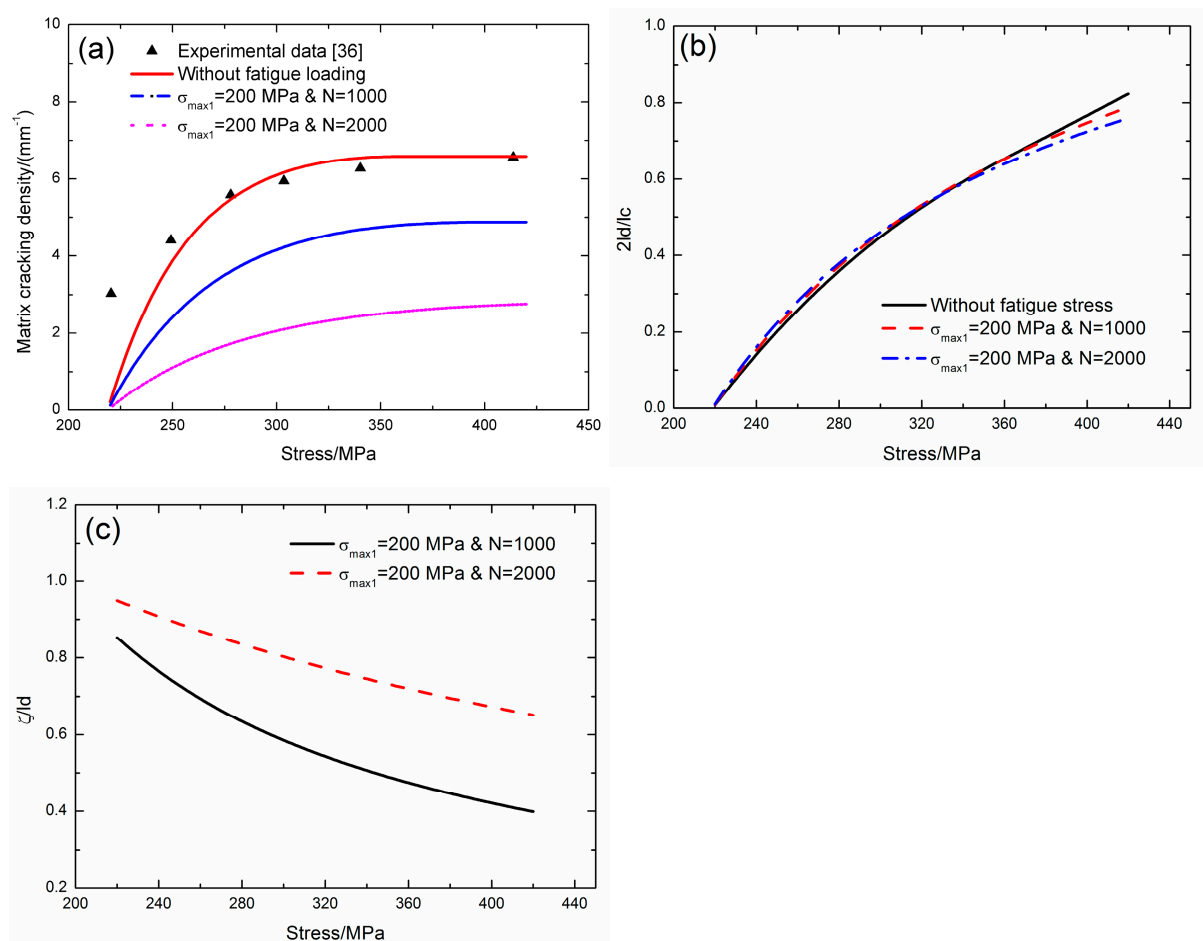


Figure 10. (a) The experimental and theoretical matrix cracking density versus applied stress curves; (b) the fiber/matrix interface debonded ratio ($2l_d/l_c$) versus applied stress curves; and (c) the fiber/matrix interface wear ratio (ζ/l_d) of unidirectional SiC/Borosilicate composite with/without fatigue loading [36].

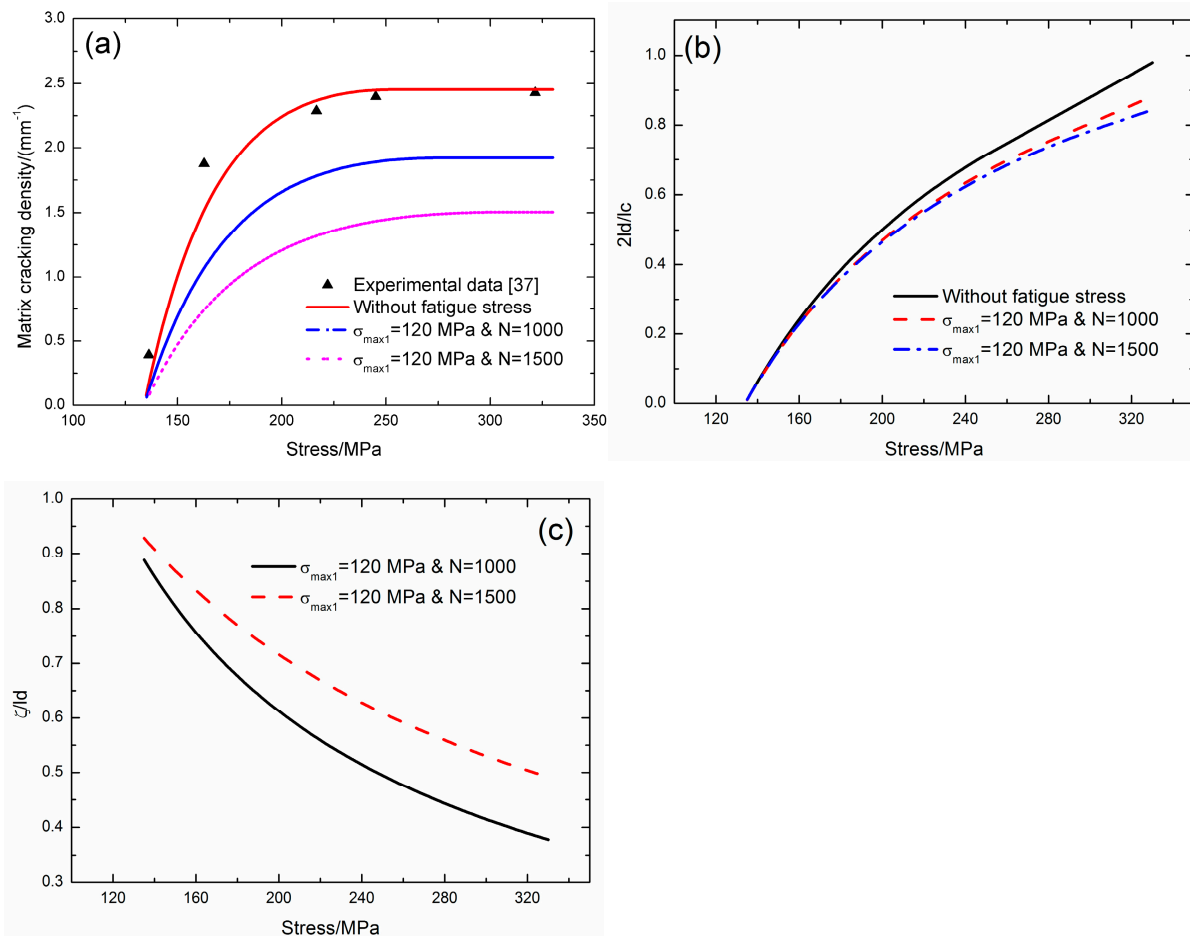


Figure 11. (a) The experimental and theoretical matrix cracking density versus applied stress curves; (b) the fiber/matrix interface debonded ratio ($2l_d/l_c$) versus applied stress curves; and, (c) the fiber/matrix interface wear ratio (ζ/l_d) of mini-SiC/SiC composite with/without fatigue loading [37].

Table 1. The material properties of SiC/CAS, SiC/SiC, SiC/Borosilicate, and mini-SiC/SiC composites.

Items	SiC/CAS [35]	SiC/CAS-II [33]	SiC/SiC [34]	SiC/Borosilicate [36]	Mini-SiC/SiC [37]
E_f /(GPa)	190	200	200	230	160
E_m /(GPa)	90	88	300	60	190
V_f	0.34	0.35	0.4	0.31	0.25
r_f /(μ m)	7.5	7.5	7.5	8	6.5
α_f /(10 ⁻⁶ /°C)	3.3	3.3	4	3.1	3.1
α_m /(10 ⁻⁶ /°C)	4.6	4.6	5	3.25	4.6
τ_i /(MPa)	10	15	50	7.6	15
ξ_d /(J/m ²)	0.4	0.1	2.8	0.2	0.4
ω	0.0001	-	0.0001	0.0001	0.0001
λ	1.3	-	1.5	2.0	1.5

Holmes and Cho [33] investigated the fatigue behavior of unidirectional SiC/CAS-II composite at room temperature. The fatigue tests were periodically interrupted to obtain the surface replicas of matrix crack spacing, and a stress of 10 MPa was maintained on the specimen while taking the replicas. The fatigue loading frequency was $f = 25$ Hz and the specimen was cycled for 25,000 cycles at different fatigue peak stresses of $\sigma_{max} = 120, 140, 160, 180, 200, 220,$ and 240 MPa. Under cyclic fatigue loading, the fiber/matrix interface shear stress degrades with applied cycles, and the initial fiber/matrix interface shear stress is $\tau_i = 20$ MPa. Figure 7 shows the experimental and predicted matrix cracking density and the fiber/matrix interface debonding versus the applies stress curves. The predicted matrix cracking

density with the initial interface shear stress of $\tau_i = 20$ MPa is much higher than the experimental data; however, the predicted matrix cracking density with low interface shear stress of $\tau_i = 15$ MPa agrees with the experimental data, which is mainly due to the interface wear mechanism.

Pryce and Smith [35] investigated the tensile behavior of unidirectional SiC/CAS composite at room temperature. The quasi-static tests were carried out using an Instron 1175 under displacement control at a cross-head speed of 0.05mm/min. The direct observations of matrix cracking were made using optical and scanning electron microscopy of the polished coupon edges. The matrix cracking density was determined by counting the number of cracks in a gauge-length of about 15mm. For the unidirectional SiC/CAS composite without cyclic fatigue loading, the matrix cracking starts from the applied stress of $\sigma_{mc} = 160$ MPa and it approaches saturation at the applied stress of $\sigma_{sat} = 288$ MPa; the matrix cracking density determined by Equation (22) increases from $\psi = 0.2$ /mm to the saturation value of $\psi = 7.0$ /mm; and, the fiber/matrix interface debonded ratio that is determined by Equation (13) increases from $2l_d/l_c = 0.7\%$ at 160 MPa to $2l_d/l_c = 79\%$ at 360 MPa. Under cyclic fatigue loading of $\sigma_{max1} = 150$ MPa and $N = 1000$, the matrix cracking density that is determined by Equation (22) increases from $\psi = 0.26$ /mm at $\sigma_{mc} = 160$ MPa to $\psi = 6.7$ /mm at $\sigma_{sat} = 284$ MPa; the fiber/matrix interface debonding ratio that is determined by Equation (13) increases from $2l_d/l_c = 0.7\%$ at 160 MPa to $2l_d/l_c = 76.1\%$ at 360 MPa; and, the fiber/matrix interface wear ratio decreases from $\zeta/l_d = 77.9\%$ at 160 MPa to $\zeta/l_d = 19.3\%$ at 360 MPa. Under cyclic fatigue loading of $\sigma_{max1} = 150$ MPa and $N = 2000$, the matrix cracking density that is determined by Equation (22) increases from $\psi = 0.12$ /mm at $\sigma_{mc} = 160$ MPa to $\psi = 4.6$ /mm at $\sigma_{sat} = 310$ MPa; the fiber/matrix interface debonding ratio that is determined by Equation (13) increases from $2l_d/l_c = 0.8\%$ at 160 MPa to $2l_d/l_c = 71.8\%$ at 360 MPa; and, the fiber/matrix interface wear ratio decreases from $\zeta/l_d = 92.9\%$ at 160 MPa to $\zeta/l_d = 42.2\%$ at 360 MPa, as shown in Figure 8.

Domergue et al. [34] investigated the damage and failure of unidirectional SiC/SiC composite at room temperature. The tensile tests were conducted with periodic unload/reload cycles, and the matrix cracking density was determined from line scans. For the unidirectional SiC/SiC composite without cyclic fatigue loading, the matrix cracking starts from the applied stress of $\sigma_{mc} = 240$ MPa and it approaches saturation at the applied stress of $\sigma_{sat} = 320$ MPa; the matrix cracking density that is determined by Equation (22) increases from $\psi = 1.1$ /mm to the saturation value of $\psi = 13$ /mm. Under the cyclic fatigue loading of $\sigma_{max1} = 200$ MPa and $N = 1000$, the matrix cracking density that is determined by Equation (22) increases from $\psi = 0.21$ /mm at $\sigma_{mc} = 240$ MPa to $\psi = 5.6$ /mm at $\sigma_{sat} = 320$ MPa; the fiber/matrix interface debonded length that is determined by Equation (13) increases from $l_d/r_f = 2.8$ at 240 MPa to $l_d/r_f = 4.2$ at 320 MPa; and, the fiber/matrix interface wear ratio decreases from $\zeta/l_d = 72.8\%$ at 240 MPa to $\zeta/l_d = 48.9\%$ at 320 MPa. Under cyclic fatigue loading of $\sigma_{max1} = 200$ MPa and $N = 2000$, the matrix cracking density that is determined by Equation (22) increases from $\psi = 0.09$ /mm at $\sigma_{mc} = 240$ MPa to $\psi = 2.8$ /mm at $\sigma_{sat} = 320$ MPa; the fiber/matrix interface debonded length that is determined by Equation (13) increases from $l_d/r_f = 7.0$ at 240 MPa to $l_d/r_f = 8.4$ at 320 MPa; and, the fiber/matrix interface wear ratio decreases from $\zeta/l_d = 89.8\%$ at 240 MPa to $\zeta/l_d = 75\%$ at 320 MPa, as shown in Figure 9.

Okabe et al. [36] investigated the tensile behavior of unidirectional SiC/Borosilicate composite at room temperature. The tensile tests were performed at a constant cross-head speed of 0.4 mm/min. The specimens were periodically stopped under tensile to replicate the matrix cracking density on the specimen surfaces using polyacetate films. For the unidirectional SiC/Borosilicate composite without cyclic fatigue loading, the matrix cracking starts from the applied stress of $\sigma_{mc} = 220$ MPa and it approaches saturation at the applied stress of $\sigma_{sat} = 360$ MPa; the matrix cracking density that is determined by Equation (22) increases from $\psi = 0.2$ /mm to the saturation value of $\psi = 6.5$ /mm; and, the fiber/matrix interface debonded ratio that is determined by Equation (13) increases from $2l_d/l_c = 0.8\%$ at 220 MPa to $2l_d/l_c = 82\%$ at 420 MPa. Under cyclic fatigue loading of $\sigma_{max1} = 200$ MPa and $N = 1000$, the matrix cracking density that was determined by Eq. (22) increases from $\psi = 0.12$ /mm at $\sigma_{mc} = 220$ MPa to $\psi = 4.8$ /mm at $\sigma_{sat} = 402$ MPa; the fiber/matrix interface debonding ratio that is determined by Equation (13) increases from $2l_d/l_c = 0.9\%$ at 220 MPa to $2l_d/l_c = 78.9\%$ at 420 MPa;

and, the fiber/matrix interface wear ratio decreases from $\zeta/l_d = 85.2\%$ at 220 MPa to $\zeta/l_d = 39.8\%$ at 420 MPa. Under cyclic fatigue loading of $\sigma_{\max 1} = 200$ MPa and $N = 2000$, the matrix cracking density that is determined by Equation (22) increases from $\psi = 0.05/\text{mm}$ at $\sigma_{\text{mc}} = 220$ MPa to $\psi = 2.7/\text{mm}$ at $\sigma_{\text{sat}} = 420$ MPa; the fiber/matrix interface debonding ratio as determined by Equation (13) increases from $2l_d/l_c = 0.9\%$ at 220 MPa to $2l_d/l_c = 75.9\%$ at 420 MPa; and, the fiber/matrix interface wear ratio decreases from $\zeta/l_d = 94.9\%$ at 220 MPa to $\zeta/l_d = 65.1\%$ at 420 MPa, as shown in Figure 10.

Zhang et al. [37] investigated the tensile damage of mini-SiC/SiC composite at room temperature. Real-time matrix crack detection of a digital microscope obtained the matrix cracking density. For the mini-SiC/SiC composite without cyclic fatigue loading, the matrix cracking starts from the applied stress of $\sigma_{\text{mc}} = 135$ MPa and it approaches saturation at the applied stress of $\sigma_{\text{sat}} = 250$ MPa; the matrix cracking density that was determined by Equation (22) increases from $\psi = 0.4/\text{mm}$ to the saturation value of $\psi = 2.4/\text{mm}$; and, the fiber/matrix interface debonded ratio that is determined by Equation (13) increases from $2l_d/l_c = 1.0\%$ at 135 MPa to $2l_d/l_c = 98\%$ at 330 MPa. Under cyclic fatigue loading of $\sigma_{\max 1} = 120$ MPa and $N = 1000$, the matrix cracking density that is determined by Equation (22) increases from $\psi = 0.05/\text{mm}$ at $\sigma_{\text{mc}} = 135$ MPa to $\psi = 1.9/\text{mm}$ at $\sigma_{\text{sat}} = 277$ MPa; the fiber/matrix interface debonding ratio as determined by Equation (13) increases from $2l_d/l_c = 1.0\%$ at 135 MPa to $2l_d/l_c = 88.2\%$ at 330 MPa; and, the fiber/matrix interface wear ratio decreases from $\zeta/l_d = 88.8\%$ at 135 MPa to $\zeta/l_d = 37.7\%$ at 330 MPa, as shown in Figure 11.

5. Conclusions

In this paper, the effect of cyclic fatigue loading on matrix multiple fracture of fiber-reinforced CMCs has been investigated. The relationships between matrix cracking, cyclic fatigue peak stress, fiber/matrix interface wear, and debonding have been established. The effects of fiber volume fraction, fiber/matrix interface shear stress, and applied cycle number on matrix multiple fracture have been conducted. Comparisons of matrix cracking with/without cyclic fatigue loading have been analyzed. The experimental matrix cracking of unidirectional SiC/CAS, SiC/SiC, SiC/Borosilicate, and mini-SiC/SiC composites with/without cyclic fatigue loading have been predicted.

- (1) When considering fiber/matrix interface wear, the matrix cracking density and the fiber/matrix interface debonding ratio decrease.
- (2) With increasing applied cycle number at a lower stress level, the matrix cracking density at a higher stress level decreases; and, the fiber/matrix interface debonded length and interface wear ratio increase.
- (3) Under the cyclic fatigue loading, the fiber/matrix interface shear stress degradation caused the lower matrix crack-density for a higher fatigued specimen, which would affect the residual modulus and the strength of fiber-reinforced CMCs.

Under cyclic fatigue loading, the matrix cracking density after fatigue loading appeared to be lower in cracking density at a higher stress level, which will affect the residual modulus and tensile strength of fiber-reinforced CMCs.

Funding: The work reported here is supported by the Fundamental Research Funds for the Central Universities (Grant No. NS2019038).

Acknowledgments: The author also wishes to the six anonymous reviewers and editors for their helpful comments on an earlier version of the paper.

Conflicts of Interest: The author declares no conflict of interest.

Nomenclature

τ_f	fiber/matrix interface shear stress in the wear region
τ_i	fiber/matrix interface shear stress in the slip region
l_d	fiber/matrix interface debonded length
ζ	fiber/matrix interface wear length
r_f	fiber radius
R	matrix radius
ρ	shear-lag model parameter
α	thermal expansion coefficient
V	volume fraction
E	Young's modulus
σ	stress
ΔT	temperature difference between fabricated and testing temperature
l_c	matrix crack spacing
ξ_d	fiber/matrix interface debonded energy
$w_f(x)$	fiber axial displacement
$w_m(x)$	matrix axial displacement
$v(x)$	relative displacement between the fiber and the matrix
τ_{io}	initial fiber/matrix interface shear stress
τ_{imin}	steady-state fiber/matrix interface shear stress
w	interface wear model parameter
λ	interface wear model parameter
U_m	matrix strain energy
σ_{cr}	critical matrix cracking stress
U_{crm}	critical matrix strain energy
ξ_m	matrix fracture energy
ψ	matrix crack density

Superscript and Subscript

f	fiber
m	matrix
c	composite

References

1. Naslain, R. Design, Preparation and properties of non-oxide CMCs for application in engines and nuclear reactors: an overview. *Compos. Sci. Technol.* **2004**, *64*, 155–170. [[CrossRef](#)]
2. Christin, F. Design, fabrication, and application of thermostructural composites (TSC) like C/C, C/SiC and SiC/SiC composites. *Adv. Eng. Mater.* **2002**, *4*, 903–912. [[CrossRef](#)]
3. Schmidt, S.; Beyer, S.; Knabe, H.; Immich, H.; Meistring, R.; Gessler, A. Advanced ceramic matrix composite materials for current and future propulsion system applications. *Acta Astronaut.* **2004**, *55*, 409–420. [[CrossRef](#)]
4. Aveston, J.; Cooper, G.A.; Kelly, A. Single and multiple fracture. In *The Properties of Fiber Composites, Conference on Proceedings*; IPC Science and Technology Press: Guildford, UK, 1971; pp. 15–26.
5. Aveston, J.; Kelly, A. Theory of multiple fracture of fibrous composite. *J. Mater. Sci.* **1973**, *8*, 352–362. [[CrossRef](#)]
6. Budiansky, B.; Hutchinson, J.W.; Evans, A.G. Matrix fracture in fiber-reinforced ceramics. *J. Mech. Phys. Solids* **1986**, *34*, 167–189. [[CrossRef](#)]
7. Chiang, Y.C. On crack-wake debonding in fiber reinforced ceramics. *Eng. Fract. Mech.* **2000**, *65*, 15–28. [[CrossRef](#)]
8. Rajan, V.P.; Zok, F.W. Matrix cracking of fiber-reinforced ceramic composites in shear. *J. Mech. Phys. Solids* **2014**, *73*, 3–21. [[CrossRef](#)]
9. Li, L. Modeling for matrix multicracking evolution of cross-ply ceramic-matrix composites using energy balance approach. *Appl. Compos. Mater.* **2015**, *22*, 733–755.
10. Li, L. Modeling first matrix cracking stress of fiber-reinforced ceramic-matrix composites considering fiber fracture. *Theor. Appl. Fract. Mech.* **2017**, *92*, 24–32.

11. Marshall, D.B.; Cox, B.N.; Evans, A.G. The mechanics of matrix cracking in brittle-matrix fiber composites. *Acta Metal. Mater.* **1985**, *33*, 2013–2021. [[CrossRef](#)]
12. McCartney, L.N. Mechancis of matrix cracking in brittle-matrix fiber-reinforced composites. *Proc. Roy. Soc. Lond.* **1987**, *409*, 329–350. [[CrossRef](#)]
13. Chiang, Y.C.; Wang, A.S.D.; Chou, T.W. On matrix cracking in fiber reinforced ceramics. *J. Mech. Phys. Solids* **1993**, *41*, 1137–1154. [[CrossRef](#)]
14. Cox, B.N.; Marshall, D.B. Crack initiation in fiber-reinforced brittle laminates. *J. Am. Ceram. Soc.* **1996**, *79*, 1181–1188. [[CrossRef](#)]
15. Deng, Y.; Li, W.; Shao, J.; Zhang, X.; Kou, H.; Ma, J.; Tao, Y.; Wang, R. Modeling the temperature-dependent non-steady first matrix cracking stress for fiber ceramic matrix composites. *J. Alloy Compd.* **2018**, *740*, 987–996. [[CrossRef](#)]
16. Ahn, B.K.; Curtin, W.A. Strain and hysteresis by stochastic matrix cracking in ceramic matrix composites. *J. Mech. Phys. Solids* **1997**, *45*, 177–209. [[CrossRef](#)]
17. Lissart, N.; Lamon, J. Damage and failure in ceramic matrix minicomposites: experimental study and model. *Acta Mater.* **1997**, *45*, 1025–1044. [[CrossRef](#)]
18. Lamon, J. Stochastic approach to multiple cracking in composite systems. *Compos. Sci. Technol.* **2009**, *69*, 1607–1614. [[CrossRef](#)]
19. Solti, J.P.; Mall, S.; Robertson, D.D. Modeling damage in unidirectional ceramic-matrix composites. *Compos. Sci. Technol.* **1995**, *54*, 55–66. [[CrossRef](#)]
20. Li, L. Effect of fiber Poisson contraction on matrix multicracking evolution of fiber-reinforced ceramic matrix composites. *Appl. Compos. Mater.* **2015**, *22*, 583–598.
21. Morscher, G.N.; Singh, M.; Kiser, J.D.; Freedman, M.; Bhatt, R. Modeling stress-dependent matrix cracking and stress-strain behavior in 2D woven SiC fiber reinforced CVI SiC composites. *Compos. Sci. Technol.* **2007**, *67*, 1009–1017. [[CrossRef](#)]
22. Xia, Z.H.; Sujidkul, T.; Niu, J.; Smith, C.E.; Morscher, G.N. Modeling of electromechanical behavior of woven SiC/SiC composites. *Compos. Part A Appl. Sci. Manuf.* **2012**, *43*, 1730–1737. [[CrossRef](#)]
23. Simon, C.; Rebillat, F.; Herb, V.; Camus, G. Monitoring damage evolution of SiC_f/[Si-B-C]_m composites using electrical resistivity: Crack density-based electromechanical modeling. *Acta Mater.* **2017**, *124*, 579–587. [[CrossRef](#)]
24. Li, L. Micromechanical modeling for tensile behavior of carbon fiber-reinforced ceramic-matrix composites. *Appl. Compos. Mater.* **2015**, *22*, 773–790.
25. Li, L. Modeling the monotonic and cyclic tensile stress-strain behavior of 2D and 2.5D woven C/SiC ceramic-matrix composites. *Mech. Compos. Mater.* **2018**, *54*, 165–178. [[CrossRef](#)]
26. Reynaud, P. Cyclic fatigue of ceramic-matrix composites at ambient and elevated temperatures. *Compos. Sci. Technol.* **1996**, *56*, 809–814. [[CrossRef](#)]
27. Fantozzi, G.; Reynaud, P. Mechanical hysteresis in ceramic matrix composites. *Mater. Sci. Eng. A* **2009**, *521*, 18–23. [[CrossRef](#)]
28. Li, L.; Reynaud, P.; Fantozzi, G. Effects of interface bonding properties on cyclic tensile behavior of unidirectional C/Si₃N₄ and SiC/Si₃N₄ composites. *Int. J. Ceram. Technol.* **2018**, *15*, 1124–1137. [[CrossRef](#)]
29. Simon, C.; Rebillat, F.; Camus, G. Electrical resistivity monitoring of a SiC/[Si-B-C] composite under oxidizing environments. *Acta Mater.* **2017**, *132*, 586–597. [[CrossRef](#)]
30. Gao, Y.C.; Mai, Y.; Cotterell, B. Fracture of fiber-reinforced materials. *J. Appl. Math. Phys.* **1988**, *39*, 550–572. [[CrossRef](#)]
31. Evans, A.G.; Zok, F.W.; McMeeking, R.M. Fatigue of ceramic matrix composites. *Acta Metal. Mater.* **1995**, *43*, 859–875. [[CrossRef](#)]
32. Li, L. Synergistic effects of fiber debonding and fracture on matrix cracking in fiber-reinforced ceramic-matrix composites. *Mater. Sci. Eng. A* **2017**, *682*, 482–490.
33. Holmes, J.W.; Cho, C. Experimental observations of frictional heating in fiber-reinforced ceramics. *J. Am. Ceram. Soc.* **1992**, *75*, 929–938. [[CrossRef](#)]
34. Domergue, J.M.; Vagaggini, E.; Evans, A.G. Relationships between hysteresis measurements and the constituent properties of ceramic matrix composites: II, Experimental studies on unidirectional materials. *J. Am. Ceram. Soc.* **1995**, *78*, 2721–2731. [[CrossRef](#)]
35. Pryce, A.W.; Smith, P.A. Behavior of unidirectional and crossply ceramic matrix composites under quasi-static tensile loading. *J. Mater. Sci.* **1992**, *27*, 2695–2704. [[CrossRef](#)]

36. Okabe, T.; Komotori, J.; Shimizu, M.; Takeda, N. Mechanical behavior of SiC fiber reinforced brittle-matrix composites. *J. Mater. Sci.* **1999**, *34*, 3405–3412. [[CrossRef](#)]
37. Zhang, S.; Gao, X.; Chen, J.; Dong, H.; Song, Y. Strength model of the matrix element in SiC/SiC composites. *Mater. Design* **2016**, *101*, 66–71. [[CrossRef](#)]



© 2019 by the author. Licensee MDPI, Basel, Switzerland. This article is an open access article distributed under the terms and conditions of the Creative Commons Attribution (CC BY) license (<http://creativecommons.org/licenses/by/4.0/>).